Structure of liquid carbon dioxide at pressures up to 10 GPa

F. Datchi,[1,][*] G. Weck,[2] A. M. Saitta,[1] Z. Raza,[1,3] G. Garbarino,[4] S. Ninet,[1] D. K. Spaulding,[2,5]
J. A. Queyroux,[1] and M. Mezouar[4]

[1]*Institut de Minéralogie, de Physique des Matériaux et de Cosmochimie (IMPMC), Sorbonne Universités - UPMC Univ. Paris 6,
CNRS UMR 7590, IRD UMR 206, MNHN, 4 place Jussieu, F-75005 Paris, France*
[2]*CEA, DAM, DIF, F-91297 Arpajon, France*
[3]*Department of Physics, Chemistry and Biology, Linköping University, SE-581 83 Linkoping, Sweden*
[4]*European Synchrotron Radiation Facility, BP 220, F-38043 Grenoble Cedex, France*
[5]*Department of Earth and Planetary Science, Harvard University, 20 Oxford St, Cambridge, Massachusetts 02138, USA*

The short-range structure of liquid carbon dioxide is investigated at pressures (P) up to 10 GPa and temperatures (T) from 300 to 709 K by means of x-ray diffraction experiments in a diamond anvil cell (DAC) and classical molecular dynamics (MD) simulations. The molecular x-ray structure factor could be measured up to 90 nm^{-1} thanks to the use of a multichannel collimator which filters out the large x-ray scattered signal from the diamond anvils. The experimental data show that the short-range structure of fluid CO_2 is anisotropic and continuously changes from a low density to a high density form. The MD simulations are used to extract a detailed three-dimensional analysis of the short-range structure over the same P-T range as the experiment. This reveals that upon compression, a fraction of the molecules in the first-neighbor shell change orientation from the (distorted) T shape to the slipped parallel configuration, accounting for the observed structural changes. The local arrangement is found similar to that of the $Pa\overline{3}$ solid at low density and to that of the $Cmca$ crystal at high density. The comparison with other simple quadrupolar liquids, either diatomic (I_2) or triatomic (CS_2), suggests that this structural evolution with density is a general one for these systems.

I. INTRODUCTION

CO_2 is undoubtedly one of the most cited and studied molecules nowadays, due to its role as a greenhouse gas in climate changes, its massive use as a solvent for material synthesis, and its impact on the global carbon cycle inside Earth. Notably, the phase diagram of CO_2 at conditions of high pressure and temperature has been the subject of many investigations [1–17], the main results of which are summarized in Fig. 1. Nonmolecular solid forms, denoted V [1], VI [2], and amorphous a-CO_2 [3] have been reported at pressures in excess of 40–60 GPa, depending on temperature. At lower pressures, four different structures of the molecular solid ($Pa\overline{3}$, $Cmca$, $P4_2/mnm$, $R\overline{3}c$) have been found depending on P-T conditions [6–8,10–12], all of which are typical arrangements for rodlike molecules with a large electric quadrupole moment like CO_2. The structural evolution of the molecular crystal with pressure may thus be understood as a balance between a more efficient packing imposed by the density increase and the constraint of minimizing the electric quadrupole-quadrupole (EQQ) interaction energy.

Experimental studies of liquid CO_2 under extreme conditions are so far mainly comprised of shock experiments [18–20]. The latter determined the Hugoniot curve from about 10 to 540 GPa and reshocked states up to ~830 GPa. An inflection of the Hugoniot curve was observed at ~34 GPa, ~3600 K and ascribed to the onset of molecular dissociation [19]. *Ab initio* molecular dynamics (AIMD) simulations [20,21] support the dissociation of CO_2 along the Hugoniot above ~30 GPa, but the nature of the dissociated liquid is debated: While Root

et al. [20] reported that CO_2 decomposes into atomic C and O, Boates *et al.* [21] found the presence of short-lived molecular species among which are CO, O_2, and C_2O_4. Note also that laser-heating DAC experiments on solid samples concluded that CO_2 dissociates into carbon and molecular oxygen at $P >$ 34 GPa and temperatures over 2000 K [14,15]. For $45 < P <$ 48 GPa and $1850 < T < 3200$ K, the AIMD simulations of Boates *et al.* [22] suggested a first-order transition in the liquid phase from the molecular to a polymeric state mainly composed of CO_3 and CO_4 units [22]. Experimental studies of the structure of liquid CO_2 would thus be valuable to assess the stability of liquid CO_2 under extreme P-T conditions. These are, however, challenging experiments, due in particular to the very low x-ray scattering cross section of this light molecule.

The structural studies of the liquid (fluid) phase reported in the literature have so far been limited to states near the triple point (0.519 MPa, 216.55 K) or in the supercritical regime close to the critical point (7.38 MPa, 304.25 K). These studies have revealed that for states with liquidlike densities, the local order in the fluid is anisotropic, with significant orientational correlations between molecules due to the anisotropic character of the intermolecular interactions [23–27]. The question thus arises whether the local structure of the molecular liquid will be modified by the density increase, as observed in the solid phase.

In this paper, we report on the evolution of the structure of liquid CO_2 at pressures up to 10 GPa using a combination of experimental and theoretical methods. Thanks to recently implemented synchrotron techniques [28], we obtain high quality experimental structure factors up to 90 nm^{-1}. We observe a continuous transformation of the short-range structure of the liquid upon compression, which, according to our MD simulations, is driven by a partial reorientation of
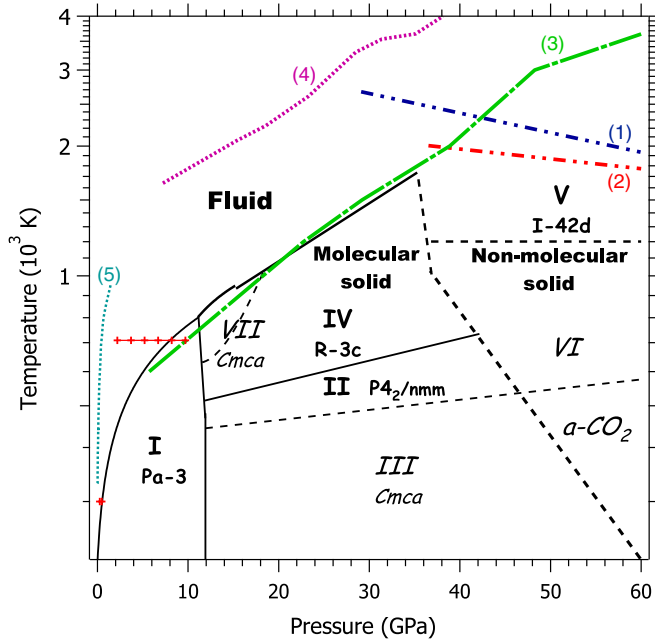
————
[*]datchi@impmc.upmc.fr

FIG. 1. Phase diagram of CO_2 compiled from literature [1–17]. Roman numbers differentiate the various solid polymorphs; the numbers in italic indicate the phases which are metastable. Solid lines are thermodynamic transition lines, while the dashed lines indicate kinetic transition lines. Lines (1) and (2) are the locus of P-T points beyond which solid CO_2 was observed to decompose in Refs. [14] and [15], respectively. Line (3) is the theoretical melting curve determined from *ab initio* simulations by Ref. [16]. Line (4) is the Hugoniot curve according to Refs. [18–20]. The temperatures of the Hugoniot have not been measured, hence we quote those determined from the *ab initio* calculations of Ref. [20]. Line (5) is the Frenkel line reported in Ref. [17]. The red lines with crosses show the two isotherms investigated in the present paper. The data points collected above 8 GPa at 709 K correspond to the overcompressed (metastable) fluid.

first-neighbor molecules from the T-shape configuration to the slipped parallel one. Interestingly, this structural evolution is similar to that occurring in the solid phase at the transition between the $Pa\bar{3}$ phase I and the *Cmca* phase VII.

II. METHODS

A. Experiments

The CO_2 samples were compressed inside membrane diamond anvil cells (DAC), using conical design (Boehler-Almax) diamond anvils [29] with x-ray apertures of 70° and culets of 0.4 to 1 mm diameter. The gaskets were made of rhenium foil indented to 80–100 μm. CO_2 was loaded in the liquid phase inside a pressure vessel. A resistive ring-shaped heater enveloping the DAC was used to heat the sample. The temperature of the heater was maintained fixed to within 2 K during the measurements. Pressure was determined using the $SrB_4O_7 : Sm^{2+}$ fluorescence sensor according to the calibration reported in Ref. [30]. Pressure uncertainties are $\sim$0.05 GPa at 300 K and $\sim$0.15 GPa at 709 K. Temperature uncertainties are below 5 K.
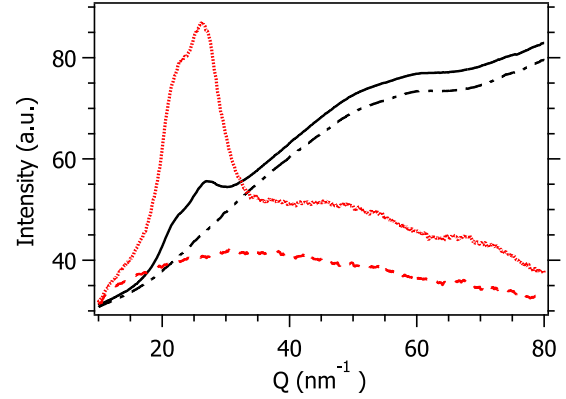

FIG. 2. Integrated x-ray diffraction patterns from a CO_2 fluid sample at 7.8 GPa, 709 K, with and without the MCC. The (red) dotted and (black) solid lines are patterns obtained with and without the MCC, respectively. The dashed and dot-dashed lines are the respective patterns from the empty cell. The intensities for the patterns obtained without MCC have been divided by 24 to scale with those measured with the MCC.

Angular-dispersive x-ray diffraction experiments (XRD) were performed on beamline ID27 of the European Synchrotron Radiation Facility (ESRF, Grenoble, France). The monochromatic x-ray beam of wavelength 0.3738 Å was focused to produce a spot size of 3×3 μm on the sample. The diffracted signal was recorded by a Mar345 image plate. Azimuthal integration of the images was performed with the fit2D [31] or Dioptas [32] softwares.

As mentioned above, x-ray diffraction of liquids composed of light elements at high pressure is a challenging task, due in particular to the low x-ray scattering cross section of the sample and the large contribution from the environment of the sample. Recently, we experimented with the use of a multichannel collimator (MCC) on samples inside a diamond anvil cell as a means to reduce the large parasitic background originating from the diamond anvils [28]. The MCC, inspired from the original design of Ref. [33], is composed of two sets of concentric slits and is positioned between the sample and the 2D detector in order to isolate a small diffracting volume around the sample [34]. This technique was successfully applied to samples of liquid hydrogen at pressures up to 5 GPa [35]. The anvil contribution to the signal is typically reduced by a factor 100 at 20 nm^{-1} and 400 at 80 nm^{-1}. As an example, Fig. 2 shows the integrated x-ray diffraction patterns collected from a liquid CO_2 sample at 7.8 GPa, 709 K and from the empty cell, when the MCC is used or not. Faint oscillations from the CO_2 sample above 35 nm^{-1} can be observed on the patterns collected with the MCC, whereas they are hidden by the large incoherent signal from the anvils when the MCC is not used.

The methodology described by Eggert *et al.* [36] was employed to extract the molecular structure factor $S_{mol}(Q)$, the molecular radial distribution function (RDF) $g_{mol}(r)$, and the average atomic density ρ_0 from the experimental data at each P-T point. We recall below the main definitions and steps of the data analysis and refer to Ref. [36] for the complete description. The measured scattering intensity $I^{meas}(Q)$ is

expressed as:

$$I^{\text{meas}}(Q) = T(Q)I^{\text{samp}}(Q) + sI^{\text{bkgd}}(Q), \qquad (1)$$

where $T(Q)$ is a transmission factor accounting for the absorption of the diamond anvils and transmission through the MCC, s is the scale factor between $I^{\text{meas}}(Q)$ and the empty-cell background scattering $I^{\text{bkgd}}(Q)$, and $I^{\text{samp}}(Q)$ is the total scattering from the sample. The latter can be written as:

$$I^{\text{samp}}(Q) = \frac{1}{N\alpha}\left[I^{\text{coh}}(Q) + N\sum_p I_p^{\text{incoh}}(Q)\right], \qquad (2)$$

where α is the normalization factor to convert the signal into atomic units, N is the number of atoms, and $I_p^{\text{incoh}}(Q)$ is the incoherent scattering from atoms of type p in the sample computed using the analytic formulas given by Hadju [37].

The molecular structure factor and radial distribution functions are then defined and related as follows:

$$S_{\text{mol}}(Q) \equiv \frac{I^{\text{coh}}(Q)}{N Z_{\text{tot}}^2 f_e^2(Q)} \qquad (3)$$

$$= S_\infty + \rho_0 \int_0^\infty [g_{\text{mol}}(r) - 1]\frac{\sin Qr}{Qr}4\pi r^2 dr \qquad (4)$$

and

$$F(r) \equiv 4\pi\rho_0 r[g_{\text{mol}}(r) - 1] \qquad (5)$$

$$= \frac{2}{\pi}\int_0^\infty [S_{\text{mol}}(Q) - S_\infty]Q \sin(Qr)dQ, \qquad (6)$$

where $Z_{\text{tot}} = Z_{\text{C}} + 2Z_{\text{O}}$ with Z_{C} and Z_{O}, the atomic numbers of C and O, respectively. $f_e(Q)$ is an effective electronic form factor defined as $f_e(Q) = (f_C(Q) + 2f_O(Q))/Z_{\text{tot}}$, where $f_X(Q)$ is the atomic form factor of atom $X = $ C or O, computed using the analytic atomic formulas given by Hadju [37]. $S_\infty = (K_C^2 + 2K_O^2)/Z_{\text{tot}}^2$, where K_X is an average effective atomic number defined as the average over the integration Q range of the function $K_X(Q) = f_X(Q)/f_e(Q)$. ρ_0 is the average atomic density.

In practice, the integral in Eq. (6) is performed up to a maximum Q value, noted Q_{max}, which depends on the experiment. Here, experimental data were collected up to 100 nm^{-1} but the rapidly decreasing signal-over-noise ratio at large Q required Q_{max} to be set from 74 nm^{-1} at the lowest density to 90 nm^{-1} at the highest densities.

The method of Ref. [36] aims at reducing the effect of experimental uncertainties on the determination of $S_{\text{mol}}(Q)$ and $g_{\text{mol}}(r)$ by performing an iterative optimization of the normalization factor α and of the scale factor s. This optimization forces the function $F(r)$ at small r, i.e., below the first intermolecular peak, to comply with the expected behavior $F(r) = F_{\text{intra}}(r) - 4\pi\rho_0$, where $F_{\text{intra}}(r)$ is the intramolecular contribution. A frozen molecule formulation is chosen for $F_{\text{intra}}(r)$, which considers the molecule as a linear rigid body with fixed carbon-oxygen and oxygen-oxygen distances of 1.163 and 2.326 Å, respectively. Since α and ρ_0 are related, they are both determined during the optimization. As noted in Ref. [36], the optimum value of ρ_0 obtained in this way is sensitive to the choice of Q_{max} at which the Fourier transform

in Eq. (6) is terminated. Here we report for ρ_0 the average value obtained by varying Q_{max} over a range of 10 nm^{-1} and use the standard deviation as a measure of the experimental uncertainty. We finally note that the presence of the MCC modifies the collected scattering intensity in a manner dependent on Q which needs to be properly taken into account, as described in Ref. [28].

It is noteworthy that the application of this method did not converge on the data collected without the MCC, due to the weakness of the sample coherent scattering for Q larger than ~35 nm^{-1}. By contrast, XRD patterns collected with the MCC successfully produced stable structure factors up to a wave vector of 90 nm^{-1}.

B. Molecular dynamics simulations

Classical molecular dynamics (MD) simulations were performed using an interaction model which considers the CO_2 molecule as a rigid linear body with a C-O bond distance of 1.163 Å and three interaction sites centered on the atoms. Site-site interactions between two molecules are modeled by pairwise-additive Lennard-Jones (LJ) and Coulombic potentials. Partial electric charges assigned to carbon ($q_c = 0.5888e$) and oxygen atoms ($q_O = -q_c/2$) are chosen to reproduce the electric quadrupole moment of the molecule. Several models of this form have been reported for CO_2; here we adopted the parameters proposed by Zhang and Duan [38], which were found superior in reproducing thermodynamic, transport, and structural experimental data over a large P-T range.

The simulations were performed with the DL_POLY_4 code [39], using a cubic box of 2048 molecules. LJ potentials cutoff was set at 15 Å. Simulations were run in the isothermal-isobaric (NPT) ensemble with a time step of 1 fs and the temperature and pressure regulated with a Nosé-Hoover thermostat/barostat. The equations of motion were integrated using the velocity Verlet algorithm and long-range electrostatic potentials summed using the smoothed particle mesh Ewald method. Simulations were equilibrated for 100 ps and then run for 1 ns in each instance.

Radial and angular distribution functions were calculated by sampling snapshots at intervals of 1 ps. The x-ray weighted molecular radial distribution function (RDF) was computed as:

$$g_{\text{mol}}(r) = \left(K_C^2 g_{\text{CC}}(r) + 4K_O^2 g_{\text{OO}}(r) + 4K_C K_O g_{\text{CO}}(r)\right)/Z_{\text{tot}}^2, \tag{7}$$

where $g_{\text{CC}}(r)$, $g_{\text{OO}}(r)$, and $g_{\text{CO}}(r)$ are, respectively, the C-C, O-O, and C-O radial distribution functions. We used the same average effective atomic numbers as for the analysis of the experimental data, $K_C = 5.69$ and $K_O = 8.15$, corresponding to a $Q_{\text{max}} = 90$ nm^{-1}. The x-ray weighted molecular structure factor was computed as in Eq. (4).

III. RESULTS

A. Experiments

XRD patterns were recorded along two isotherms at 300 and 709 K, up to 0.47 and 9.7 GPa, respectively. These isotherms are represented as red lines with crosses on the phase diagram
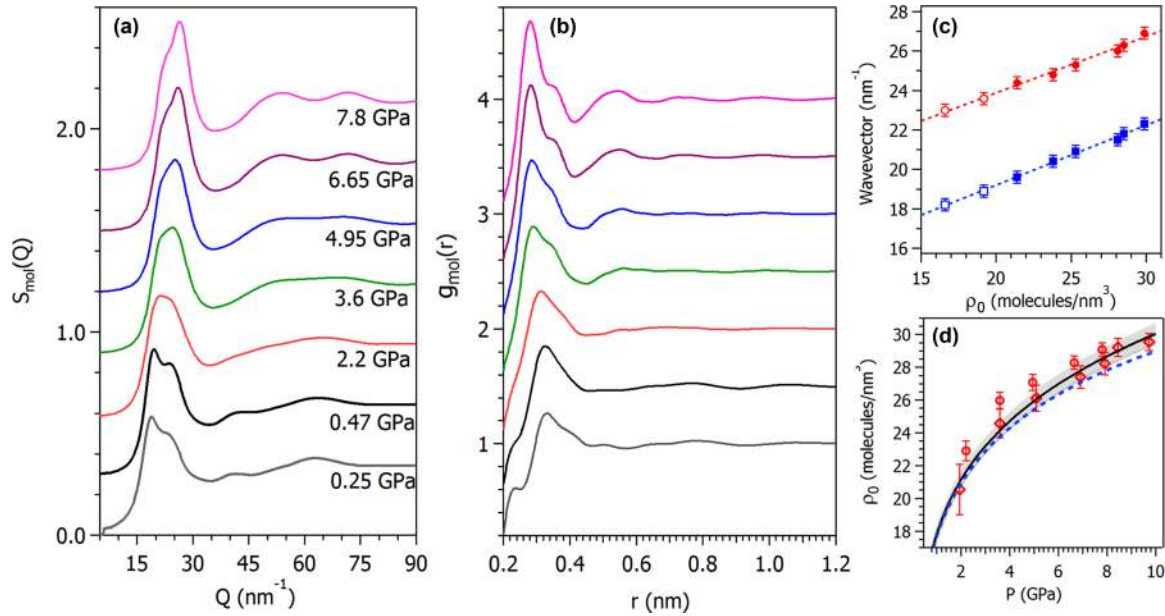
FIG. 3. Experimental results from our x-ray diffraction study of fluid CO_2. Panels (a) and (b) show, respectively, the molecular structure factor and radial distribution functions obtained at the indicated pressures. The curves are offset by 0.3 and 0.5, respectively, for clarity. The temperature was 709 K except for the patterns at 0.25 and 0.47 GPa, which were recorded at 300 K. In panel (c), the wave-vector positions of the two components of the MDP are plotted against the average atomic density. Open and solid symbols are experimental data at 300 and 709 K, respectively, and dashed lines are linear fits. In panel (d), open symbols are the average atomic densities at 709 K obtained from the experiments (circles and diamonds distinguish two different experiments), the dashed line is the 709 K isotherm given by our MD simulations, and the solid line is the same isotherm (with related 2% uncertainty shown by the light gray zone) derived from the equation of state of Ref. [9].

in Fig. 1. We observe that all the data points collected in the supercritical region are located on the right side of the Frenkel line reported in Ref. [17] [line (5) in Fig. 1] and thus correspond to liquidlike states. Note also that the freezing point of CO_2 at 709 K is 8 GPa, thus the data collected above this pressure correspond to the overcompressed (metastable) liquid.

The evolutions of the experimental $S_{mol}(Q)$ and $g_{mol}(r)$ with pressure are presented in Figs. 3(a) and 3(b), respectively. At all pressures, the structure factor of fluid CO_2 is dominated by a main diffraction peak (MDP) near 20 nm^{-1} followed by faint and broad oscillations at larger wave vectors. The MDP appears to be composed of at least two components, which contrasts with the single peak observed in simple liquids and is the signature of an anisotropic fluid structure [40]. With increasing density, not only do the peaks of $S_{mol}(Q)$ move towards higher Q, as expected, but its shape also visibly changes. In particular, there is a progressive inversion of intensity between the two components of the MDP: While the lower Q component is more intense below 1 GPa, it is outgrown by the one at higher Q at 3.6 GPa and above. This is a strong indication that the fluid structure undergoes modifications upon densification.

Figure 3(c) shows the evolution with the atomic density of the wave-vector position of the two components of the MDP, noted $Q_{m,1}$ and $Q_{m,2}$. To extract these positions, we fit the function $I^{coh}(Q)$ defined in Eqs. (2) and (3) using Voigt profiles. $I^{coh}(Q)$ was preferred over $S_{mol}(Q)$ as it goes to 0 at large Q. For density we use the equation of state of Ref. [9], which agrees very well with present experiments (see below), in order to smooth out the fluctuations due to experimental

uncertainties. Both $Q_{m,1}$ and $Q_{m,2}$ appear to vary linearly with ρ_0 over the probed density range. In particular the data points at 300 K line up very well with those at 709 K, which indicates that the temperature effects on the structure are small compared to those of density.

There are also significant changes in the evolution of $g_{mol}(r)$ with density, as seen in Fig. 3(b). First, the broad and asymmetric first intermolecular peak of $g_{mol}(r)$ at low pressure increases in intensity by 33% and progressively decomposes into two components, indicating that the nearest neighbors arrange in a more anisotropic fashion in the high density fluid. Second, the correlations at larger r become more important at high density.

The average atomic densities obtained in the present experiments along the 709 K isotherm are plotted against pressure in Fig. 3(c) and compared to the experimental equation of state (EOS) of Ref. [9]. The latter is based on sound velocity measurements up to 8 GPa and 700 K, and its uncertainty was estimated to be 2%. The agreement is good, within mutual error bars of both experiments. A comparison with the shocked fluid densities cannot be made as the P-T range of the present experiments does not overlap with those of shock experiments [18–20]. The monotonous increase and absence of discontinuity in $\rho_0(P)$ is consistent with the fact that CO_2 remains a molecular system under these thermodynamic conditions and confirms that the structural changes occur continuously with pressure.

Our experimental data thus provide clear evidence that the structure of liquid CO_2 continuously evolves from a low-density to a high-density form on increasing pressure. Unfortunately, the interpretation of the data in terms of

structure is limited because $g_{mol}(r)$ is a weighted sum of three site-site RDFs [see Eq. (7)] which cannot be extracted from a single diffraction pattern. In the following, we compare our experimental data to MD simulations and use the latter to extract a microscopic description of the liquid structure.

B. Molecular dynamics simulations

MD simulations were performed at 0.1, 0.2, and 0.47 GPa at 300 K and at seven pressures from 0.9 GPa to 10 GPa at 650 K. Additional simulations were done at selected P-T points from the experimental data set to allow for direct comparison. We note that all probed states are liquid over the time of the simulations, although the stable state of CO_2 at 10 GPa, 650 K is the solid phase I. This is because the nucleation of the solid phase in computer simulations is a rare event, enabling us to probe overcompressed states of the liquid.

The potential of Zhang and Duan (ZD) used in our simulations was shown to well reproduce the low-pressure thermodynamic and transport properties and the neutron diffraction patterns of fluid CO_2 from 0.833 to 1.089 g/cc [38]. To test the applicability of this potential in the GPa range, we compared the computed densities to experimental values. As seen in Fig. 3(c), the ZD model predicts lower densities than the EOS of Ref. [9], but the difference remains within 3% below 10 GPa, i.e., close to experimental uncertainties. We also compared the predicted site-site radial distribution functions (SS-RDF) $g_{CC}(r)$, $g_{CO}(r)$, and $g_{OO}(r)$ to those obtained using first-principles calculations [41,42] at the density of 19.17 molecules/nm^3 (1.4 g/cc), corresponding to a pressure of 0.47 GPa at 300 K. The close agreement between the two sets of SS-RDF (see Supplementary Fig. S1 in Ref. [43]) indicates that, as far as the fluid structure is concerned, the predictability of the classical MD simulations with the ZD model is comparable to that of *ab initio* modeling in this pressure range.

The calculated molecular structure factors and radial distribution functions are compared to experimental results in Fig. 4. The agreement is fairly good over the full pressure range, both in amplitude and peak positions (note that the Q and r scales have been slightly adjusted for the point at 7.8 GPa, 709 K to account for the density difference between experiment and simulations—see caption of Fig. 4). Notably, the simulations exhibit the same inversion of intensity ratio for the two components of the MDP with increasing pressure. The peaks of $g_{mol}(r)$ appear broader in the experiment than in the simulations, which is a well-known effect of the finite truncation of the Fourier transform of $S_{mol}(Q)$ [36]. Note that the peak at 0.233 nm comes from the *intra*molecular-OO correlations. It appears as a sharp peak in the simulated $g_{mol}(r)$ because the molecule is modeled as a rigid body with a fixed intramolecular-OO distance. The broadening of this peak in the experimental $g_{mol}(r)$ is entirely due to the finite truncation of the Fourier transform, since this peak is imposed in the data analysis through the formulation of $F_{intra}(r)$ (see Sec. II A). It also appears less clearly on increasing pressure as it becomes convoluted with the first *inter*molecular peak whose position shifts to lower r.

The fact that the present simulations catch the most important features of the experimental $S_{mol}(Q)$ and $g_{mol}(r)$
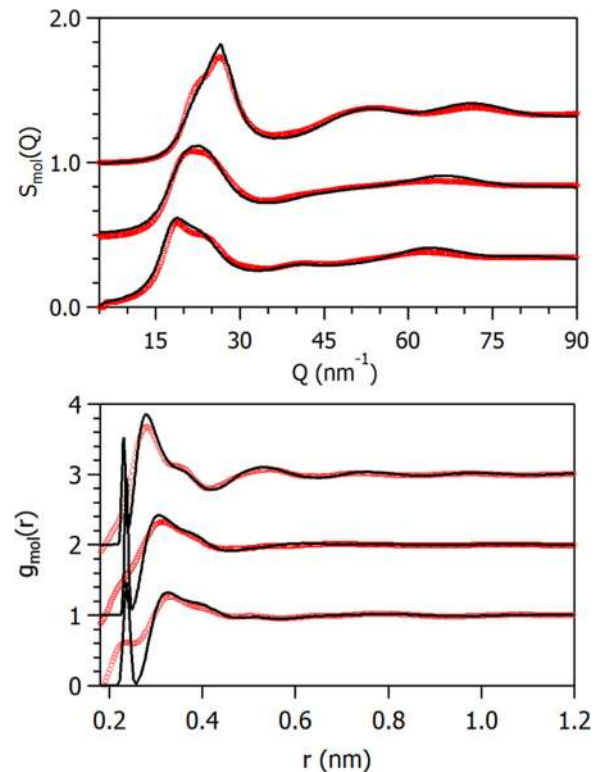

FIG. 4. Comparison between the MD simulated and experimental molecular structure factor (top) and molecular radial distribution function (bottom) at selected P-T points. Experimental data and MD simulations are shown with red circles and black lines, respectively. Note that the low-r part of $g_{mol}(r)$ (below 0.2 nm) is not shown as it only contains the fixed *intra*molecular-CO peak at 0.1163 nm. In both panels, the bottom curves are for 0.25 GPa, 300 K, the middle ones are for 2.2 GPa, 709 K, and the top ones are for 7.8 GPa, 709 K. Between each curves, offsets of 0.3 and 1 are applied for $S_{mol}(Q)$ and $g_{mol}(r)$, respectively. To account for the slight density difference at 7.8 GPa, 709 K between experiment and simulations, the Q-scale and r-scale have been multiplied by 1.02 and 0.98, respectively, for this P-T point.

without any fitting gives confidence that they provide a good approximation of the structure of the real system. It is possible that a better match to the experimental data could be obtained by an ad-hoc fitting of the potential parameters [27] or by other methods, but we don't believe this would significantly change the conclusions drawn hereafter.

The SS-RDF given by the simulations at two representative thermodynamic conditions, namely 0.47 GPa, 300 K ($\rho_0 = 19.17$ molecules/nm^3 or 1.4 g/cc) and 10 GPa, 650 K ($\rho_0 = 29.19$ molecules/nm^3 or 2.13 g/cc), are presented in Fig. 5. The shapes of these RDF are largely affected by the density increase. In particular, the first peak of $g_{CC}(r)$, which is a singlet at low pressure peaked at 0.4 nm, splits into two components located at 0.3 and 0.36 nm at 10 GPa. The number of molecules in the first-neighbor shell, as estimated by the relation $n = 4\pi\rho \int_0^{r_m} r^2 g_{CC}(r)\,dr$ where r_m is the first minimum of $g_{CC}(r)$, only slightly increases from 13.2 at the lower density to 13.6 at the higher one. The first peak of $g_{CO}(r)$ presents a shoulder on the low r side at 0.47 GPa and progressively decomposes in two well-resolved oscillations
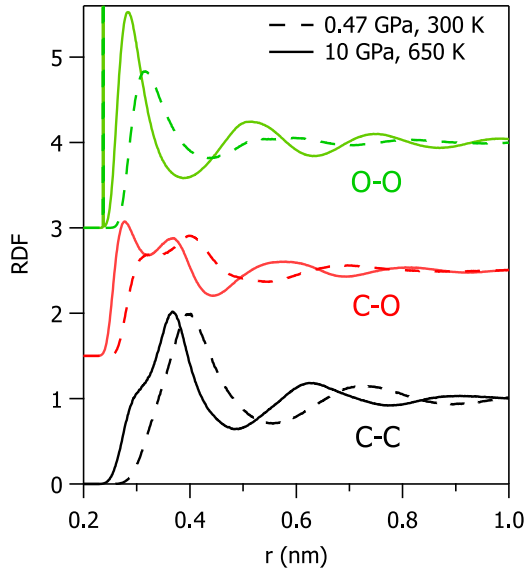
FIG. 5. Site-site radial distribution functions of fluid CO_2, as obtained from MD simulations, at 0.47 GPa-300 K (dashed lines) and 10 GPa-650 K (solid lines). The C-O and O-O RDF are offset by 1.5 and 3, respectively.

with increasing pressure. The sharpening of the peaks in $g_{OO}(r)$ also attests to a more structured liquid at high density. From the site-site RDF, it is possible to assign the two components of the first intermolecular peak of $g_{mol}(r)$: The first oscillation peaked at 0.288 nm at 7.8 GPa mainly arises from O-O and C-O correlations, while the second one at ∼0.37 nm is composed of C-O and C-C correlations.

A three-dimensional description of the structure requires analyzing the angularly resolved molecular distributions. As in Ref. [44], we first determined the probability that, given a molecule at the origin, a molecule is found at the distance r and polar angle θ_r, defined as the angle between the axis of the central molecule and the line connecting the carbon atoms of the two molecules [see inset of Fig. 6(a)]. The probability maps $P(r, \theta_r)$ obtained at 0.47 GPa, 300 K and 10 GPa, 650 K are shown in Figs. 6(a) and 6(b), respectively.[1] At the lower pressure, $P(r, \theta_r)$ presents a maximum at $r = 0.39$ nm and $\theta_r = 90°$, and two smaller peaks at about 40 and 140° at the same distance (see also Supplementary Fig. S2 in Ref. [43]). The larger peak, on one hand, corresponds to molecules whose center, *viz* carbon atom, preferentially occupies the equatorial plane of the central molecule; the smaller peaks, on the other hand, correspond to molecules near the poles of the central molecules. To assess the mutual orientation of these molecules, we then look at the distributions of the angle θ_2 between the line connecting the centers of the two molecules and the axis of the second, and of the angle θ_m between the two molecular

axes. For the equatorial molecules, i.e., with $\theta_r = 90 \pm 5°$, the distributions show at $r = 0.39$ nm a broad peak at $\theta_m = 90°$ and two well-defined symmetric peaks at $\theta_2 \approx 33°$ and $\theta_2 \approx 147°$ [see Fig. 6(c) and Supplementary Fig. S3 in Ref. [43]]. This tells us that not only the carbon atoms but also oxygen atoms tend to align close to the equatorial plane and orient in a (distorted) T-shape configuration with respect to the central molecule. For the polar molecules, i.e., with $\theta_r = 40 \pm 5°$, the θ_2 and θ_m maps also reveal a clear preference for the T-shape configuration [Fig. 6(c)].

We next turn our attention to the structure at 10 GPa, 650 K. The $P(r, \theta_r)$ map reveals two subshells of first-neighbor molecules at the respective distances of 0.3 and 0.36 nm, consistent with the splitting of $g_{CC}(r)$ noted above. The molecules at $r = 0.3$ nm are most probably found at θ_r angles of ∼66° and ∼114°, while in the second subshell, they are more likely found around θ_r values of 37°, 90°, and 143°. By analyzing the θ_2 and θ_m maps at each of these angles [see Fig. 6(d) and Supplementary Fig. S4 in Ref. [43]], we find, on one hand, that the molecules at $r = 0.3$ nm are now parallel to the central molecule, and more precisely in the "slipped parallel" (s-//) configuration where the molecule is translated along its axis by half the molecule length. The molecules at $r = 0.36$ nm, on the other hand, are oriented in the T-shape configuration like at the lower density. The densification of fluid CO_2 thus imposes the reorientation of part of the molecules in the first-neighbor shell from the distorted T shape to the s-// configuration. The number of such molecules, as estimated by integrating $4\pi \rho_0 r^2 g_{CC}(r)$ up to 0.32 nm, is ∼1.7, which leaves ∼11.9 molecules in the T-shape configuration.

IV. DISCUSSION

The above results show that at the lowest densities probed in this study there is a clear prevalence for the (distorted) T-shape configuration in the first coordination shell of liquid CO_2. Theoretical studies of simple quadrupolar liquids [45,46] have shown that this arrangement originates from the electric quadrupole-quadrupole (EQQ) interactions, since the larger the quadrupole is, the higher is the probability to find T-shape configurations. Our findings agree very well with previous works based on neutron diffraction data [25] or *ab initio* calculations [41] at similar densities (14.9–19.17 molecules/nm³). The fact that the same molecular configurations are obtained with *ab initio* calculations and with the classical potential used in the present paper gives further credit in the ability of the latter to describe the structure of liquid CO_2.

As noted in Ref. [41], this configuration of molecules in the first shell is remarkably similar to that found in the $Pa\bar{3}$ crystal structure of phase I. In the latter indeed, each CO_2 molecule has 12 first neighbors at the same C-C distance ($r = 0.398$ nm at the melting point 0.57 GPa, 300 K [47]), six of which are in the equatorial plane and the other six are around the poles [see Fig. 6(e)]. All of them are in a distorted T-shape configuration with $\theta_2 = 35°$ for equatorial molecules and $\theta_2 = 90°$ for polar molecules. As shown in Figs. 6(a) and 6(c), the angular positions and orientations of molecules in the $Pa\bar{3}$ solid are well correlated with the probability peaks

---

[1]Angular distributions were computed by measuring angles between pairs of molecules, followed by construction of a histogram normalized to the total number of molecules over the spanned range of distance and angles. For the histograms constructed for a given value of θ_r, all molecules with a θ_r of the specific value plus or minus 5° were used to evaluate θ_2 or θ_m.
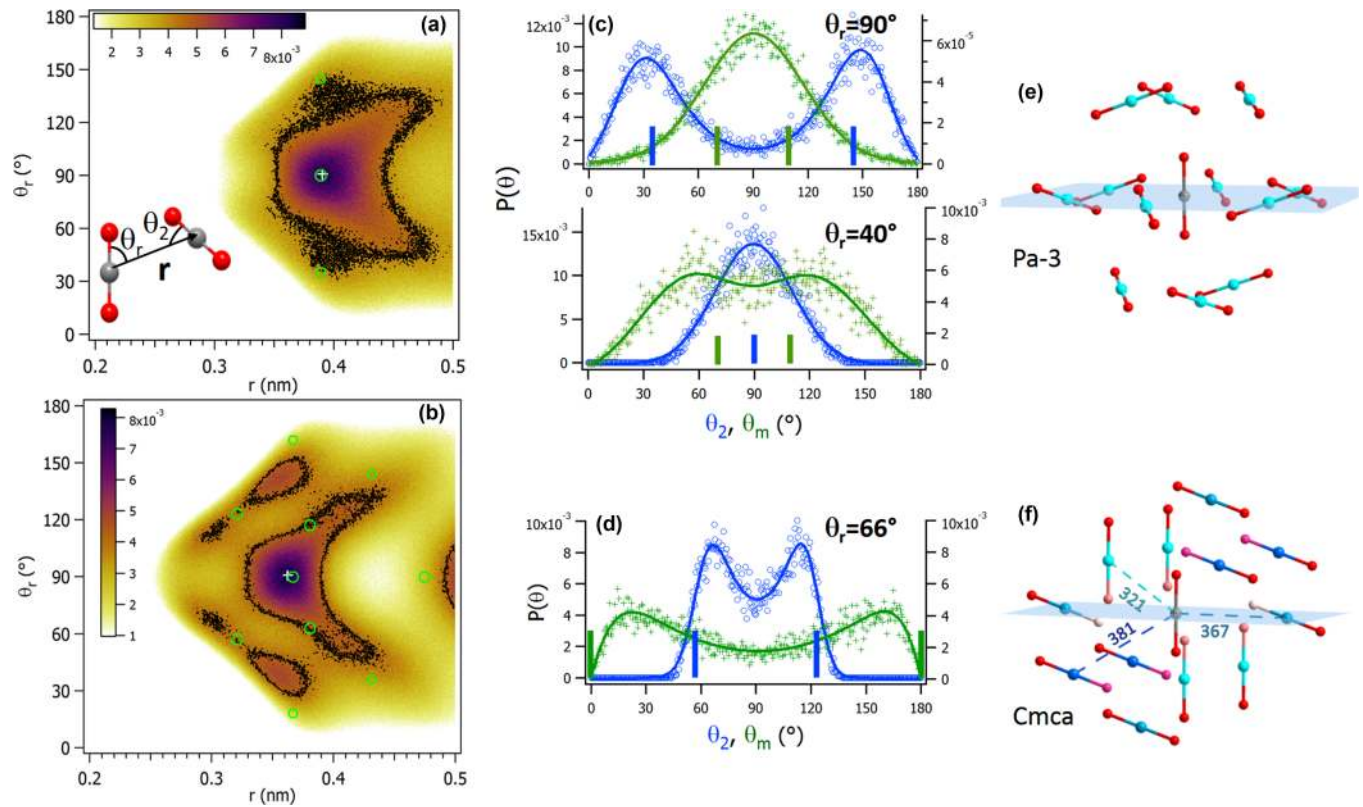
FIG. 6. Angular distributions of nearest neighbor molecules at 0.47 GPa, 300 K [(a),(c)] and 10 GPa, 650 K [(b),(d)] from MD simulations. The inset of (a) shows the definition of θ_r and θ_2 angles. (a), (b): probability maps for the polar angle θ_r. The cross shows the position of the maximum; black dots indicate the contours at half maximum. The green circles are the positions of molecules in the $Pa\bar{3}$ (a) or $Cmca$ (b) crystal. (c), (d): Distributions of the angles θ_2 (circles, left axis) and θ_m (crosses, right axis) at $r = 0.39$ nm (c) and $r = 0.3$nm (d) for indicated θ_r values. The lines are fits using (asymmetric) Gaussian peaks. The bars are the respective angles in the $Pa\bar{3}$ (c) or $Cmca$ (d) crystal. (e), (f): Representations of the nearest neighbors in the $Pa\bar{3}$ (e) and $Cmca$ (f) structures. All carbon atoms are at the same distance (0.398 nm) from the central molecule in $Pa\bar{3}$; for $Cmca$, C-C distances are indicated in pm and C atoms of neighbor molecules are colored in different blue shades (lighter is closer).

in the fluid. The short-range structure of liquid CO_2 near the melting line at 300 K can thus be viewed as a disordered version of the $Pa\bar{3}$ solid. It must be kept in mind though that this description is based on a *static* view of the *most probable* configuration of the first shell, which thus neglects all the other possible but *less probable* configurations.

On increasing density, we observe that the probability to find first-neighbor molecules which are oriented in the s-// configuration progressively increases, such that the first coordination shell divides in two subshells of s-// and T-shape oriented molecules, respectively. This is easily understood, as the s-// arrangement enables a closer contact and thus a larger overlap, between molecules, thus accommodating the increase in density. The persistence of T-shape configurations as most probable however shows that EQQ interactions still have a large influence on the structure of the fluid. A similar evolution has been evidenced in computer simulations of liquid iodine [48]: On increasing density along an isotherm at 805 K, the population of s-// configurations increases sharply above the critical density, while that of T-shape configurations remains approximately constant. We may thus expect that this effect of density on the liquid structure can be generalized to other diatomic or triatomic liquids with large quadrupole moments.

The structural evolution of liquid CO_2 with pressure has a striking resemblance to that observed for the solid phase. Indeed, the $Pa\bar{3}$ solid transforms into the $Cmca$ structure (phase III) above ∼12 GPa at 300 K [8], and the fluid crystallizes in the same structure (phase VII) above 810 K at 11.5 GPa [10]. As in $Pa\bar{3}$, the asymmetric unit of $Cmca$ is composed of a single molecule, hence all the molecules have the same environment. Using the lattice parameters at 12.4 GPa, 726 K [10], the four nearest neighbors of a given molecule in $Cmca$ are in the s-// configuration at the C-C distance $r = 0.321$ nm [see Fig. 6(f)]. Further apart, there are four molecules at $r = 0.367$ nm and four more at $r = 0.381$ nm, all oriented in the distorted T-shape configuration. The resemblance to the fluid structure at 10 GPa can be appreciated from Fig. 6(b), where the angular positions of the molecules in $Cmca$ are indicated on the fluid $P(r,\theta_r)$ map: These positions are all located near regions where molecules in the fluid have a large probability to be found. There are, however, notable differences: First, the number of molecules in the s-// configuration in the fluid (∼1.7) is reduced compared to the crystal (4); second, these molecules can approach closer to each other in the fluid, even though the solid is 12.5% denser at 12.4 GPa, which can be understood by the disordered nature of the fluid phase.
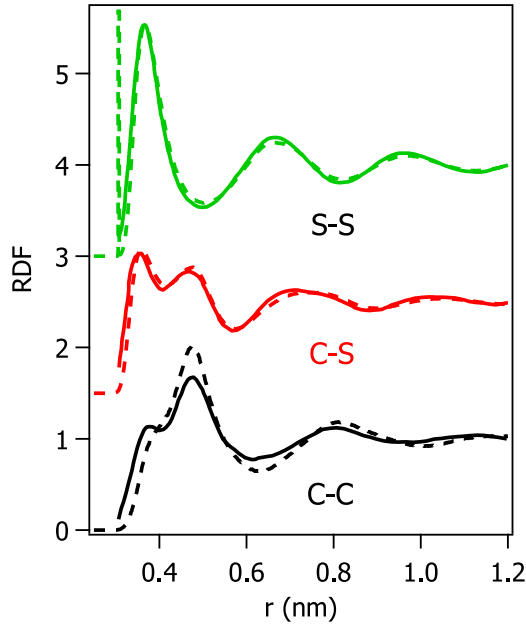
FIG. 7. The site-site radial distribution functions of fluid CS_2 at 1.2 GPa, 300 K (solid lines, digitized from Fig. 5 of Ref. [49]) are compared to those of fluid CO_2 at 10 GPa, 650 K (dashed lines) as obtained from MD simulations. The distances in CO_2 have been scaled to correct for the density difference between the two fluids, i.e., r values have been multiplied by $(\rho_{CO_2}/\rho_{CS_2})^{1/3} = 1.295$.

We also found it instructive to compare the structure of the high-pressure liquid CO_2 to that of liquid CS_2. The CS_2 molecule has the same shape, albeit a longer C-S bond length of 1.554 Å and an electric quadrupole moment which is 20% smaller than that of CO_2 and opposite.[2] The structure factor of liquid CS_2 has been determined by XRD up to 1.2 GPa at 300 K, i.e., close to its freezing pressure (1.3 GPa) [49]. These authors showed that a potential of the same form as that presently used for CO_2 gives a very good account of the experimental data. In Fig. 7, we compare the SS-RDF of CS_2 at 1.2 GPa with those of CO_2 at 10 GPa, 650 K, after scaling the distances in CO_2 to correct for the density difference between the two fluids. The similarities are striking: There is almost a perfect match between $g_{OO}(r)$ and $g_{SS}(r)$ and a very good one between $g_{CO}(r)$ and $g_{CS}(r)$. The $g_{CC}(r)$ RDFs are more unlike at first glance, however both show a split first peak which mainly differ by the splitting and intensity ratio between the two components, both being larger in CS_2. Unfortunately, a detailed analysis of the angular distributions is missing for CS_2. The similarities between the SS-RDFs and the fact that both systems can be modeled with the same type of potential suggest that the short-range structure of CS_2 near freezing at 300 K is similar to that of CO_2 at 10 GPa. Under this assumption, we may assign the first and second component of the first peak of $g_{CC}(r)$ to molecules in s-// and T-shape

---

[2]According to Ref. [50], the values of the electric quadrupole moment Θ of CO_2 and CS_2 are, respectively, -1.5×10^{-39} C.m^2 and 1.2×10^{-39}. Note that the sign of Θ has no influence on EQQ interactions since the latter are proportional to Θ^2 (Ref. [45]).

configurations, respectively. The larger splitting between the two components is then easily explained by the longer length of the CS_2 molecule, and the larger probability to find molecules in the s-// configuration likely originates from the smaller quadrupole moment of CS_2 and thus weaker influence of the EQQ interactions in the intermolecular potential. As a matter of fact, the contribution of s-// molecules is readily apparent in the $g_{CC}(r)$ RDF of CS_2 at ambient pressure [27,49], unlike the low-density CO_2 fluid. The number of s-// molecules continuously grows in CS_2 up to 1.2 GPa, which is consistent with the general trend outlined above for quadrupolar liquids. It is also interesting to mention that CS_2 crystallizes at 300 K in the same *Cmca* structure as CO_2 at high P-T, which substantiates the idea that the short range structure of the liquid near freezing resembles that of the solid phase in these systems.

V. CONCLUSION

In summary, we have presented experimental data for the x-ray structure factor of fluid CO_2 at pressures up to 10 GPa, which extends the density range of previous determinations by a factor ∼2. These experiments were made possible thanks to the use of a multichannel collimator recently implemented for angular-dispersive x-ray diffraction in a diamond anvil cell [28]. After liquid H_2 [35], liquid CO_2 proved to be a good test case for this setup as the diffracted coherent signal is very weak for $Q > 35$ nm^{-1} and requires an excellent rejection of the Compton scattering of the diamond anvils to be detected.

The experimental molecular structure factors $S_{mol}(Q)$ and radial distribution functions $g_{mol}(r)$ from 0.25 GPa to 9.7 GPa evidenced a continuous structural transformation of fluid CO_2 with pressure from a low density to a high density form. To elucidate the nature of this transformation, we performed MD simulations based on a classical pair potential including LJ and Coulombic terms with the parameters recommended by Ref. [38]. This interaction model was found competitive with respect to *ab initio* calculations and to well reproduce the experimental evolution of $S_{mol}(Q)$ of $g_{mol}(r)$ with pressure and was thus used as a basis for the description of the short-range structure of liquid CO_2 and its evolution with density. The main findings are: (1) in the low-density liquid below 1.4 g/cc, the most probable configuration in the first-neighbor shell is the (distorted) T shape, which agree well with previous studies; (2) on increasing density, the proportion of molecules in s-// configuration increases sharply, and comprises ∼12.5 % of the first-neighbor molecules at 2.13 g/cc; (3) this structural evolution presents similarities with the $Pa\bar{3}$-$Cmca$ transition in the solid, although proceeding through continuous steps and starting at a lower pressure; (4) the density-induced increase of s-// configurations appears as a general feature of quadrupolar liquids of diatomic and linear triatomic molecules.

It can also be expected that the pressure-induced transformations of the local structure has a substantial impact on the dynamics of the system, in particular the rotational and translational diffusions, and consequently on the solvent properties of fluid CO_2. This could be of particular relevance for the interaction of CO_2 with minerals and the properties

of geological fluids in Earth's upper mantle and thus deserves further investigations.

Finally, extending the present experiments to higher P-T conditions appears within reach of the present technique and its future extension. This could reveal other interesting phenomena such as the liquid-liquid transition between molecular and nonmolecular CO_2 predicted by theory [22] and could provide valuable information on the nature of the dissociated liquid evidenced by shock experiments.

[1] V. Iota, C. S. Yoo, and H. Cynn, Science **283**, 1510 (1999).

[2] V. Iota, C. S. Yoo, J. H. Klepheis, Z. Jenei, W. Evans, and H. Cynn, Nat. Mater. **6**, 34 (2006).

[3] M. Santoro, F. A. Gorelli, R. Bini, G. Ruocco, S. Scandolo, and W. A. Crichton, Nature (London) **441**, 857 (2006).

[4] V. Iota and C. S. Yoo, Phys. Rev. Lett. **86**, 5922 (2001).

[5] C. S. Yoo, V. Iota, and H. Cynn, Phys. Rev. Lett. **86**, 444 (2001).

[6] A. Simon and K. Peters, Acta Crystallogr. Sect. B **36**, 2750 (1980).

[7] R. T. Downs and M. S. Somayazulu, Acta Crystallogr. Sect. C **54**, 897 (1998).

[8] K. Aoki, H. Yamawaki, M. Sakashita, Y. Gotoh, and K. Takemura, Science **263**, 356 (1994).

[9] V. M. Giordano, F. Datchi, and A. Dewaele, J. Chem. Phys. **125**, 054504 (2006).

[10] V. M. Giordano and F. Datchi, EPL **77**, 46002 (2007).

[11] F. Datchi, B. Mallick, A. Salamat, G. Rousse, S. Ninet, G. Garbarino, P. Bouvier, and M. Mezouar, Phys. Rev. B **89**, 144101 (2014).

[12] F. Datchi, V. M. Giordano, P. Munsch, and A. M. Saitta, Phys. Rev. Lett. **103**, 185701 (2009).

[13] F. Datchi, B. Mallick, A. Salamat, and S. Ninet, Phys. Rev. Lett. **108**, 125701 (2012).

[14] O. Tschauner, H. K. Mao, and R. J. Hemley, Phys. Rev. Lett. **87**, 075701 (2001).

[15] K. D. Litasov, A. Goncharov, and R. J. Hemley, Earth Planet. Sci. Lett. **309**, 318 (2011).

[16] A. Teweldeberhan, B. Boates, and S. A. Bonev, Earth Planet. Sci. Lett. **373**, 228 (2013).

[17] C. Yang, V. V. Brazhkin, M. T. Dove, and K. Trachenko, Phys. Rev. E **91**, 012112 (2015).

[18] G. L. Schott, High Press. Res. **6**, 187 (1991).

[19] W. J. Nellis, A. C. Mitchell, F. H. Ree, M. Ross, N. C. Holmes, R. J. Trainor, and D. J. Erskine, J. Chem. Phys. **95**, 5268 (1991).

[20] S. Root, K. R. Cochrane, J. H. Carpenter, and T. R. Mattsson, Phys. Rev. B **87**, 224102 (2013).

[21] B. Boates, S. Hamel, E. Schwegler, and S. A. Bonev, J. Chem. Phys. **134**, 064504 (2011).

[22] B. Boates, A. Teweldeberhan, and S. A. Bonev, Proc. Nat. Acad. Sci. USA **109**, 14808 (2012).

[23] A. K. Adya and C. J. Wormald, Mol. Phys. **74**, 735 (1991).

[24] S. Chiappini, M. Nardone, F. P. Ricci, and M. C. Bellissent-Funel, Mol. Phys. **89**, 975 (1996).

[25] P. Cipriani, M. Nardone, and F. Ricci, Physica B (Amsterdam) **241-243**, 940 (1997).

[26] L. Temleitner and L. Pusztai, J. Phys. Condens. Matter **19**, 335203 (2007).

[27] J. Neuefeind, H. E. Fischer, J. M. Simonson, A. Idrissi, A. Schöps, and V. Honkimäki, J. Chem. Phys. **130**, 174503 (2009).

[28] G. Weck, G. Garbarino, S. Ninet, D. Spaulding, F. Datchi, P. Loubeyre, and M. Mezouar, Rev. Sci. Instrum. **84**, 063901 (2013).

[29] R. Boehler and K. D. Hantsetters, High Press. Res. **24**, 391 (2004).

[30] F. Datchi, A. Dewaele, P. Loubeyre, R. L. Toullec, Y. L. Godec, and B. Canny, High Press. Res. **27**, 447 (2007).

[31] A. Hammersley, S. O. Svensson, M. Hanfland, A. Fitch, and D. Hausermann, High Press. Res. **14**, 235 (1996).

[32] C. Presher and V. B. Prakapenka, High Press. Res. **35**, 223 (2015).

[33] K. Yaoita, Y. Katayama, K. Tsuji, T. Kikegawa, and O. Shimomura, Rev. Sci. Instrum. **68**, 2106 (1997).

[34] G. Morard, M. Mezouar, S. Bauchau, M. Lvarez-Murga, J. L. Hodeau, and G. Garbarino, Rev. Sci. Instrum. **82**, 023904 (2011).

[35] G. Weck, G. Garbarino, P. Loubeyre, F. Datchi, T. Plisson, and M. Mezouar, Phys. Rev. B **91**, 180204 (2015).

[36] J. H. Eggert, G. Weck, P. Loubeyre, and M. Mezouar, Phys. Rev. B **65**, 174105 (2002).

[37] F. Hadju, Acta Crystallogr. Sect. A **28**, 250 (1972).

[38] Z. Zhang and Z. Duan, J. Chem. Phys. **122**, 214507 (2005).

[39] I. T. Todorov, W. Smith, K. Trachenko, and M. T. Dove, J. Mater. Chem. **16**, 1911 (2006).

[40] N. H. March and M. P. Tosi, *Introduction to Liquid State Physics* (World Scientific, London, 2002).

[41] M. Saharay and S. Balasubramanian, J. Phys. Chem. B **111**, 387 (2007).

[42] S. Balasubramanian, A. Kohlmeyer, and M. L. Klein, J. Chem. Phys. **131**, 144506 (2009).

[43] See Supplemental Material at http://link.aps.org/supplemental/10.1103/PhysRevB.94.014201 for supplementary figures S1–S4.

[44] P. Cipriani, M. Nardone, F. Ricci, and M. Ricci, Mol. Phys. **99**, 301 (2001).

[45] W. B. Street and D. J. Tildesley, Proc. R. Soc. London A **355**, 239 (1977).

[46] A. De Santis, R. Frattini, D. Gazzillo, and M. Sampoli, Mol. Phys. **60**, 21 (1987).

[47] V. M. Giordano, F. Datchi, F. A. Gorelli, and R. Bini, J. Chem. Phys. **133**, 144501 (2010).

[48] A. De Santis, A. Gregori, and D. Rocca, Mol. Phys. **85**, 271 (1995).

[49] S. Yamamoto, Y. Ishibashi, Y. Inamura, Y. Katayama, T. Mishina, and J. Nakahara, J. Chem. Phys. **124**, 144511 (2006).

[50] M. Battaglia, A. Buckingham, D. Neumark, R. Pierens, and J. Williams, Mol. Phys. **43**, 1015 (1981).